

## **EFFECT OF SWEEP ANGLE ON THE VORTICAL FLOW OVER DELTA WINGS AT AN ANGLE OF ATTACK OF 10°**

JAMES BRETT\*, ANDREW OOI

Department of Mechanical Engineering, The University of Melbourne, Australia

\*Corresponding Author: brettjd@unimelb.edu.au

### **Abstract**

CFD simulations have been used to analyse the vortical flows over sharp edged delta wings with differing sweep angles under subsonic conditions at an angle of attack of 10°. RANS simulations were validated against experimental data for a 65° sweep wing, with a flat cross-section, and the steadiness of the flow field was assessed by comparing the results against unsteady URANS and DES simulations. To assess the effect of sweep angle on the flow field, a range of sweep angles from 65° to 43° were simulated. For moderate sweep wings the primary vortex was observed to detach from the leading edge, undergoing vortex breakdown, and a weaker, replacement, "shadow" vortex was formed. The shadow vortex was observed for sweep angles of 50° and less, and resulted in reduced lift production near the wing tips loss of the stronger primary vortex.

Keywords: CFD, Delta Wing, Sweep Angle, Vortical Flow

### **1. Introduction**

Delta wing aircraft develop strong leading edge vortices which provide significant lift, and ensures the flow remains attached at higher angles of attack than a traditional wing. This allows delta wing aircraft to operate over a wide range of angles attack. Over the last decade, delta wing aircraft have received additional research attention due to an increase in delta wing unmanned aerial vehicles. Many of these aircraft are using delta wings with moderate to low sweep angles, allowing them to maximise the surface area of the wing in a relatively compact package.

The physics of delta wing vortices is described by Dèlery [1]. The vortex structure over delta wing at moderate angle of attack or higher consists of a large, primary vortex, and at higher angles of attack, smaller secondary vortex and an even weaker tertiary vortex between the primary and secondary vortices as illustrated in Fig. 1. The

**Nomenclatures**

$C_p$	Coefficient of pressure
$C_R$	Root chord, metres
Re	Reynolds Number
$y^+$	Non-dimensionalised wall distance

**Greek Symbols**

$\alpha$	Angle of attack, deg.
$\lambda$	Sweep angle, deg

**Abbreviations**

UCAV	Unmanned Combat Aerial Vehicle
------	--------------------------------

secondary vortex occurs very close to the leading edge, while the primary vortex sits above the wing, slightly behind the secondary vortex. The smaller tertiary vortex is weak enough that it is not seen in most studies.

The behaviour of the leading edge vortex (LEV) depends on many factors. Above a critical angle of attack, vortex breakdown occurs, significantly reducing the lift generated by the vortex. The camber of the delta wing has also been shown to affect the leading edge vortices by Younis et al. [2]. The sweep angle of the wing has a strong effect, with moderate to low sweep angle wings displaying different behaviour to higher sweep angle wings. This is apparent in the wealth of research on the 1303 Unmanned Combat Aerial Vehicle (UCAV) design [3-5] which found that at above a moderate angle of attack of  $8.5^\circ$  the wing undergoes a phenomena called pitch break, with drastic reduction in pitch moment resulting from the primary leading edge vortex detaching from the leading edge of the wing, and forming a trailing vortex.

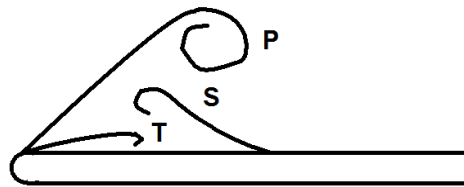


**Fig. 1. A Sketch of a Spanwise Cut Plane through a Delta Wing Cross-section Showing the Primary (P), Secondary (S) and Tertiary (T) Vortices. The Flow Direction is Out of the Page.**

Several authors have carried out experimental investigations of the effect of sweep angle over delta wings. Optimising the sweep angle of delta wing is of obvious interest when looking into delta wing aircraft. Traditionally most research into sweep angles has concentrated on slender (high sweep angle, typically  $\lambda \geq 65^\circ$ ) delta wings for this reason, as they produce more stable flows, and are best suited to supersonic flows where delta wings are commonly employed. There is much less research into the flow over non-slender, or moderate sweep angle, delta wings. The term moderate does not have a consistently employed definition, when referring to sweep angles, but it typically is used for wings with a sweep

angle somewhere in 30-50° range. Moderate sweep angle wings have received an increased research interest in the last decade, in part because they are being employed in military aircraft, especially unmanned aerial vehicles, for which high speed, supersonic flight is less crucial than being able to produce a large amount of lift in a compact package when performing long surveillance missions.

Some of the earliest published works into the effect of sweep angles is that of Earnshaw [6], and Earnshaw and Langford [7]. These studies looked at the flow over delta wings with sweep angles of 70° and 65°, and also considered variations to the shape of the wing tip. Ol and Gharib [8] compared two different sweep angles, 65° and 50° at low Reynolds Numbers (the highest tested was  $8.5 \times 10^3$  and  $1.54 \times 10^4$  for the two geometries respectively). They used a combination of dye visualisation, and stereoscopic particle image velocimetry (SPIV) to examine the leading edge vortex location and structure over a range of angles of attack. For angles of attack below 10° the flows were very similar. At higher angles of attack the 50° sweep wing exhibited an earlier onset of vortex breakdown, and a "large scale collapse of the rolled-up LEV structure" which led to a vortex without a significant axial velocity peak in the core.

To date a wide range of delta wing aircraft have been investigated under a range of flight conditions. Examinations of the effect of sweep angle have only covered limited ranges of angle of attack, at low Reynolds numbers. This investigation aims to identify the effect of sweep angle on the leading edge vortex, and identify the sweep angle at which the flow structure changes from the stable high sweep angle bound vortex, to the detached vortical flow observed with moderate sweep wings like the 1303 UCAV. The changes flow structure will be related to the changes in hydrodynamic forces on the delta wing.

## 2. Computational Method

Numerical simulations were carried out using the commercial Computational Fluid Dynamics (CFD) software package FLUENT 13. The wing platform modeled was based on a 65° sharp edged delta wing with a flat cross section, which has experimental data published by Chu and Luckring [9] and Konrath et al. [10]. A sketch of this wing is shown in Fig. 2. Sweep angles of less than 65° were achieved by stretching this geometry in the span wise direction. This resulted in an increase in wing area, and hence total lift. The root chord was kept consistent to ensure a constant Reynolds number.

The Reynolds-Averaged Navier-Stokes (RANS) equations were solved to produce a time averaged solution at minimal expense. The validity of RANS was tested by comparing simulations to URANS and DES methods at two sweep angles (45° and 65°). The unsteadiness in the vortices was found to be very small (outside of the downstream wake), especially for the 65° sweep wing. Comparisons of instantaneous vortex structures, wall shear lines and surface pressure distributions demonstrated that the RANS solver was producing a sufficiently accurate solution at minimal computational expense.

The  $k-\omega$  SST turbulence model of Menter [11] was employed, due to its ability to accurately model the flow in regions of adverse pressure gradients and separated flow [12]. Tests of various turbulence models on the 1303 UCAV by

Arthur and Petterson [4] found that the  $k-\omega$  SST model resulted in high accuracy simulations. The  $k-\omega$  SST model is also not highly sensitive to minor fluctuations in the far field turbulence specification, unlike the standard  $k-\omega$  model. For DES simulations the Spalart-Allamaras [13] formulation was used.

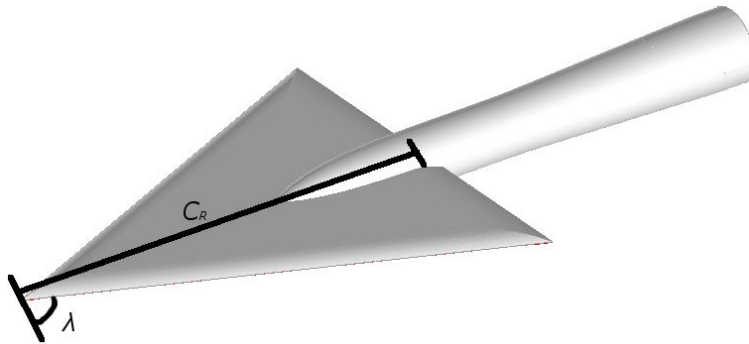


**Fig. 2. Sketch of the Geometry Used for the Vortex Wing. In this Case the Sweep Angle,  $\lambda$ , is  $65^\circ$ . The Wing Thickness is 3.4% of the Root Chord. The Curvature of the Cross-Section near the Leading Edge is Detailed in [9].**

Six different sweep angles were considered,  $65^\circ$ ,  $60^\circ$ ,  $55^\circ$ ,  $50^\circ$ ,  $45^\circ$ , and  $43^\circ$ . The smallest sweep angle was restricted to  $43^\circ$  due to the large surface area of low sweep wings and the memory limitations of the computer used to generate the mesh. This range of angles covers the original unmodified geometry ( $65^\circ$ ), and extends below the  $47^\circ$  sweep angle of the 1303 UCAV, on which pitch break has previously been observed. An unstructured tetrahedral mesh was used, with adaptive meshing employed to better resolve the vortices. The full wing was modelled, instead of just using one half with a symmetry plane to allow for unsteady motions across the symmetry plane in the URANS and DES simulations. The adaptive mesh refinement was employed to dynamically refine the mesh cells in areas where the curvature of pressure was highest. The adaptive mesh refinement algorithm assesses the curvature of pressure, multiplied by local mesh scale every 20 iterations, and refines cells where the value is too high. This methodology results in improved mesh resolution around the vortex cores and other regions of interest. Mesh independence studies were used on the  $65^\circ$  case to determine a mesh resolution that accurately resolves the flow. Mesh refinement involved refining different regions of the mesh, including the surface mesh density, degree of adaptive refinement, boundary prism layer resolution, and mesh density in different regions around the wing. Each simulation result was inspected and compared to higher and lower levels of mesh resolution to find a mesh which accurately tracked the primary vortex location and the surface shear topology of the flow. Three prism layers were used to model the boundary layer with the standard  $k-\omega$  wall function, and  $y^+$  values of less than 300 across the entire surface. High levels of mesh refinement were included in regions of possible fluctuating flow to better capture vortex positions and any unstable motions in the URANS and DES simulations.

The final mesh resolution produced results that were largely mesh independent, with some diffusion of small vortices being the only noticeable mesh effect, and provided good validation against experimental data. Figure 3

shows a cut plane of the mesh through the plane of symmetry. Mesh element sizes were kept the same for all sweep angles, however the smaller sweep angle meshes has more elements due to the increased surface area of the wing. For the  $65^\circ$  wing, the total number of mesh cells after refinement was approximately 4.5 million cells and for the  $43^\circ$  wing the total number of cells was approximately 6 million cells. Simulations to assess the effect of sweep angle were carried out at a Reynolds number of 2.85 million, based on the mean aerodynamic chord, and a Mach number of 0.25. The flow was treated as incompressible due to the low Mach number for the majority of the simulation, however validation cases were performed at higher Mach numbers using a compressible solver. The assumption of incompressibility at Mach 0.25 was confirmed by performing both compressible and incompressible simulations on the  $65^\circ$  sweep wing. Resulting pressure fields and wall shear lines revealed no significant differences. Second order discretisation schemes were used for all variables.

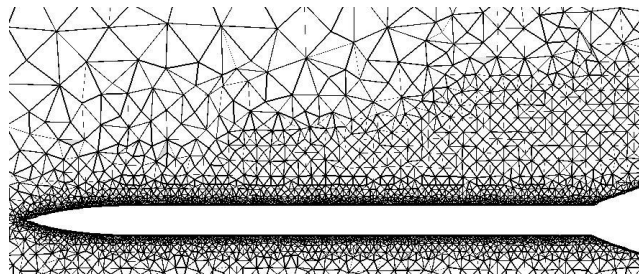


**Fig. 3. Cut plane of the Unstructured Mesh through the Symmetry Plane of the Wing. Air flow Travels from Left to Right. The Front of the Sting is Visible on the Right-hand Side of the Image. Regions with Large Curvature of Pressure, such as the Leading Edge Vortex are Further Refined by the Adaptive Mesh Refinement.**

Except for the validation cases, all the simulations were performed at an angle of attack of  $10^\circ$ . This angle was selected based on results for the  $47^\circ$  sweep 1303 UCAV aircraft. Previous studies [3,5] had shown that the leading edge vortex behaviour underwent significant changes at an angle of attack between  $8^\circ$  and  $9^\circ$ . An angle of attack of  $10^\circ$  was therefore used to allow this behaviour to be observed as a function of sweep angle. Validation cases were selected that were close to  $10^\circ$ .

### 3. Validation

Previously published results by Brett et al. [5] using the  $47^\circ$  sweep 1303 UCAV geometry indicated that RANS simulation provide accurate data for moderate sweep angle delta wings at low to moderate angles of attack and subsonic Mach numbers. To assess the accuracy with high sweep angle wings validation studies were carried out on the  $65^\circ$  wing against experimental data from Chu [9] at an angle of attack of  $10.3^\circ$ , Mach number of 0.401 and a Reynolds number of 6 million. The experimental data included force data and pressure tap measurements. The pressure taps were located on the upper and lower surfaces in

five spanwise arrays, at  $x$  distances of 20, 40, 60, 80 and 95% of the root chord measured from the apex of the wing.

Experimental error estimates were calculated and quoted in the report, so it can be used as a valuable comparison case. For the values being used as a comparison in this report the error in the coefficients of pressure and normal force are  $\pm 0.012$ . It should be noted that although the uncertainties here are the same (to two significant figures), for both the pressure and normal force coefficients, this is a coincidence, for other Mach numbers they were found to be significantly different.

Figure 4 shows a comparison of the pressure tap data with the RANS simulation data. The five span wise arrays have been offset on the plot to clearly distinguish each array. Away from the leading edge vortex good agreement is observed, however there is a significant difference in the measured low pressure footprints under the leading edge vortex for some of the spanwise arrays. The simulated flow predicts a less intense, wider, low pressure footprint underneath the leading edge vortex. The agreement improves as the vortex moves downstream and grows in size, at the final array the agreement is vastly improved. It should be noted that these arrays differ in scale, due to the sweep of the wing, the leading arrays (the upper most arrays in the figure) represent a much shorter physical length, and therefore a smaller diameter vortex.

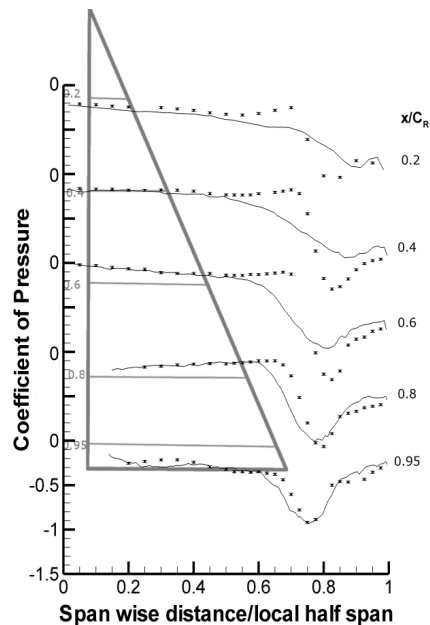


**Fig. 4. Comparison of Coefficient of Pressure Measurements at  $\alpha = 10.3^\circ$ , Mach 0.401 and  $Re=6.0$  Million between RANS Simulation (Solid Line) and Experimental Results from Pressure Tap Data (Symbols) Published by [2].**

These results indicate that although the model is predicting the formation of a leading edge vortex in the correct location, either the size of the vortex, or the impact of the vortex on the local pressure field is not as accurate. The improvement in accuracy as

the vortex propagates downstream and grows in size, suggests that this may be a result of mesh not being sufficiently fine to adequately resolve the smaller vortex without grid effects causing the vorticity to be diffused over a wider area.

The same case was simulated with additional mesh refinement, resulting in approximately twice the number of mesh elements (9.3million instead of 4.5million). This reduced the discrepancy near the leading edge, but had no significant effect on the downstream vortex structure. Results are shown in Fig. 5. Compared to the lower mesh size in Fig. 4, an improved calculation of the vortex footprint is observed, particularly near the middle of the leading edge, when the vortex is still relatively small. The larger mesh sizes around the vortex core are seen to diffuse the vortex pressure distribution resulting in a larger spread of the suction peak. For the very early stages of the leading edge vortex formation the peak is still diffused, which indicated that to accurately resolve the early stages of the vortex formation, a very large number of mesh elements would be required. However the base mesh size, without the extra levels of refinement, used for this simulation still captures the key vortex structures well, and results in more manageable mesh sizes especially for low sweep wings with a larger surface area.

The normal force coefficient was calculated by including the forces on the wing and the section of the sting referred to as the "model sting" by Chu and Luckring [9]. For the RANS simulation the calculated coefficient was 0.415. Chu and Luckring measured the normal force coefficient for the wing to be  $0.420 \pm 0.012$  under the simulated conditions, which compares well with the value from our simulations.

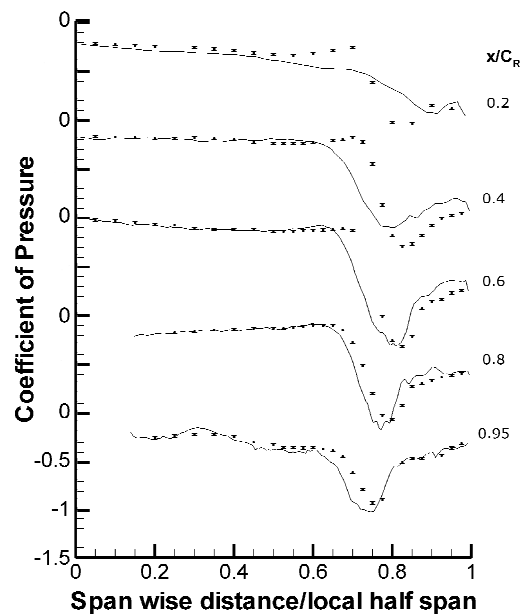


**Fig. 5. Comparison of Coefficient of Pressure Measurements at  $\alpha = 10.3^\circ$ , Mach 0.401 and  $Re=6.0$  Million between High Density Mesh RANS Simulation (Solid Line) and Experimental Results from Pressure Tap Data (Symbols) Published by [2]. Total Mesh Size is more than Twice that Shown in Fig. 4.**

Additional verification studies were undertaken against pressure sensitive paint data published by [10]. The case compared was a Reynolds number of 2 million, Mach 0.4 and an angle of attack of  $10.1^\circ$ . Contours of coefficient of pressure ( $C_p$ ) are shown in Fig. 6. The two sets of results show good agreement on the location of the leading edge vortex, however there are some notable differences. The pressure-sensitive paint results have a higher suction under the leading edge vortex on the upstream half of the wing, less disturbances near the trailing edge, and a higher coefficient of pressure on the sting. The discrepancies with upstream half of the leading edge vortex are consistent with those observed when comparing the simulated results against Chu and Luckring's experiment, and are again likely caused by a lack of resolution resulting in a dispersed vortex footprint. The difference on the sting is likely due to slightly different sting arrangement used for the experiments, compared to the sting used by Chu and Luckring which was reproduced for our simulations. Other possible sources of difference include numerical inaccuracy and dissipation with the simulation, slight variations in Reynolds number and angle of attack, and inaccuracy from the pressure-sensitive paint. Considering all the available sources of error the agreement between the two sets of results is very promising, and indicates that the simulations are accurately resolving the key features of the flow with the exception of excessive diffusion of small vortices.

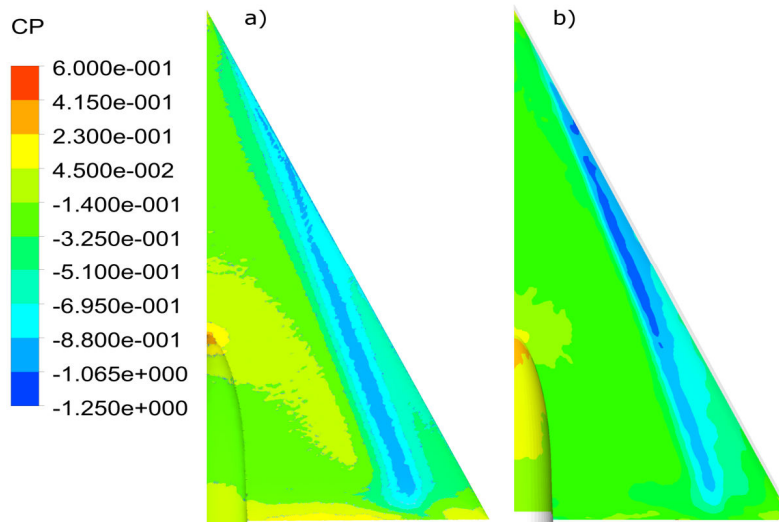


**Fig. 6. Comparison of Coefficient of Pressure Contours  $\alpha=10.1^\circ$ , Mach 0.4 and  $Re=2.0$  Million between (a) RANS Simulation and (b) Experimental Results from Pressure-Sensitive Paint. Experimental Data from VFE-2 [15]**

The use of a steady RANS turbulence model significantly reduces the computational time compared to unsteady simulations however it can lead to inaccurate results in cases the flow features significant fluctuations with time. The positive agreement with experimental data suggests that this is not the case with

the vortices above the delta wing used in this paper at moderate angles of attack. However, to provide more rigorous validation of the steady state data, additional simulations were undertaken. For both the 65° and 45° sweep wings the same case was run using steady RANS, unsteady RANS (URANS) and DES (Detached Eddy Simulation).

Instantaneous instances of the resulting pressure fields and vortex structures are shown in Fig. 7, and reveal minimal variations between time instances. The unsteady simulations led to fluctuations of pressure with time near the trailing edge, but very little variation of the primary vortex. The unsteadiness of the primary vortex was assessed by locating the minimum pressure point inside the vortex core on chord wise cut planes. For the 65° case the minimum pressure point in the vortex varied in small cluster of 3-4 grid points depending on the cut plane. The 45° sweep wing similarly fluctuated between a pair of grid points on the planes that were examined. Minor pressure fluctuations as a function of time were more prominent on the 45° sweep wing, but the vortex structure was unchanged.

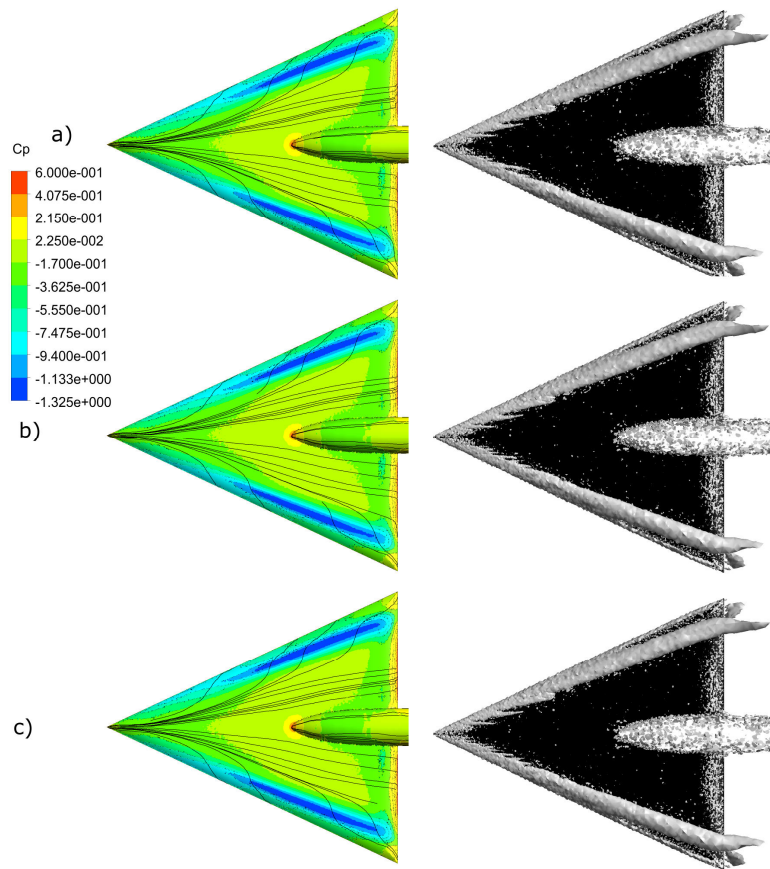


**Fig. 7. Instantaneous Wall Shear Lines and Pressure Contours (Left) and Iso-surfaces of  $\lambda-2$  (Right) at  $\alpha=10^\circ$  and Mach 0.25 for Three Different Numerical Models. a) RANS, b) URANS, and c) DES.**

#### 4. Effect of Sweep Angle

As the sweep angle was decreased the leading edge vortex was observed to generate a stronger suction near the apex of the wing, and a reduced effect near the wing tip. This can be seen from the contours of the coefficient of pressure in Fig. 8. The wall shear lines also reveal signs of recirculation near the wing tip for angles of  $50^\circ$  and less. This is consistent with the expected flow pattern in the absence of the strong leading edge vortex, which would maintain an attached flow over the leading edge.

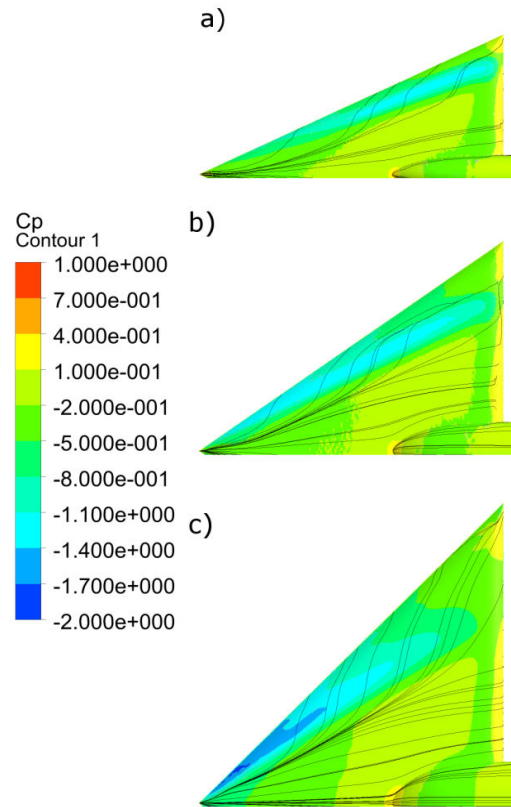


**Fig. 8. Coefficient of pressure and wall shear lines at  $\alpha=10^\circ$  and Mach 0.25 for three different sweep angles. a)  $65^\circ$  b)  $55^\circ$  c)  $45^\circ$ .**

At sweep angles of  $50^\circ$  and less the primary vortex was observed to detach from the leading edge on the outer wing. The point of detachment moved further upstream for the small sweep angles, as shown by the location of the bend of the red lines in Fig. 9. The red line in the figure shows the change in orientation of the vortex when it detaches from the leading edge. After detachment, the vortex (visualised using the  $\lambda$ -2 criterion of Jeong and Hussain [14]) maintains some span wise velocity orientation and then trails directly downstream after passing the trailing edge.

The detached vortex has less intensity, and a larger size, as is apparent from the cross sections of the  $\lambda$ -2 criterion shown in Fig. 10. This figure shows cut planes of  $\lambda$ -2 criterion, taken at 10% intervals along the chord of the wing. The larger primary vortex and a smaller, more concentrated vortical structure formed by the separation of the shear layer, are labelled A and B respectively. A smaller vortex is observed forming between the leading edge and the primary vortex on the 45° sweep wing, labelled C. This shall be referred to as the "shadow" vortex in this paper, as it is both weaker than the primary vortex, and approximately follows the path the primary vortex would take if it did not detach. The shadow vortex is acting as a replacement primary vortex after the primary vortex detaches, and rotates in the same direction.

The loss of primary vortex intensity and the formation of the shadow vortex occur further upstream than the apparent point of vortex detachment shown in Fig. 9. This reveals an interesting insight into the physics behind the onset of the detachment of the primary vortex. As the sweep angle is reduced, the incident component of the free stream velocity normal to the leading edge is increased. This results in the vortex sheet that stretches from the leading edge, and rolls up into the primary vortex being stretched further towards the centre line. It appears that at some critical angle of sweep and attack combination the vortex sheet becomes over stretched and an additional vortex roll up occurs, forming the shadow vortex, resulting in the onset of vortex bursting in the primary vortex. This bursting is characterised by a reduced vorticity in the vortex core, coupled with a growth in diameter.

Due to the weaker strength of the shadow vortex there is a significant reduction in vortex induced lift in regions where the primary vortex has detached from the leading edge vortex. This can be seen in the pressure plots in Fig. 9, after vortex detachment the pressure over the outer portion of the wing is significantly higher. This results in the net lift force being generated further forward on the low sweep delta wings, generating a net positive pitch moment about the centre of volume of the wing.

From the examinations of the  $\lambda$ -2 cross sections it appears that the formation of a distinct shadow vortex occurs at about the same stream wise location as the primary vortex shows signs of bursting. The primary vortex appears to rapidly increase in cross sectional area at around the 50-60% chord mark. This is much further upstream than the point of vortex detachment marked in Fig. 9. This implies that any attempt to prevent the vortex from detaching from the leading edge, and therefore maintain the lift over the outer wing, needs to begin before the vortex visibly detaches. A control mechanism would need to prevent the stretching of the vortex sheet, and the formation of the shadow vortex, rather than trying to maintain the vortex attachment near the trailing edge.

## 5. Effect on Hydrodynamic Forces

At the simulated angle of attack the sweep angle has a marked effect on the hydrodynamic forces acting on the delta wing, as shown by the pitching moment and force coefficients in Table 1. For lower sweep angles the low pressure region under the leading edge vortex does not extend all the way to the wing tip, and is significantly stronger near the apex of the wing as shown in Fig. 8, which results in the pitching moment increasing with decreasing sweep angle.

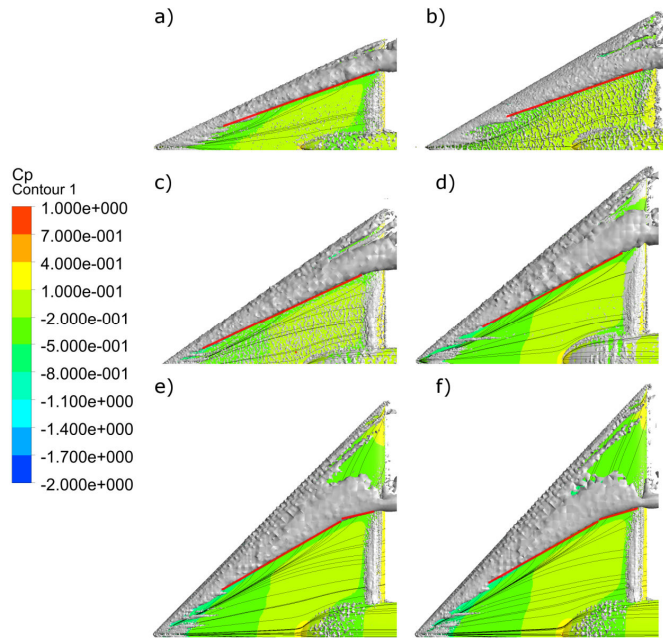


**Fig. 9. Iso-surface of  $\lambda$ -2 Criterion, over Coefficient of Pressure and Wall Shear Lines at  $\alpha=10^\circ$  and Mach 0.25 for Six Different Sweep Angles. a)  $65^\circ$  b)  $60^\circ$  c)  $55^\circ$  d)  $50^\circ$  e)  $45^\circ$  f)  $43^\circ$ .**

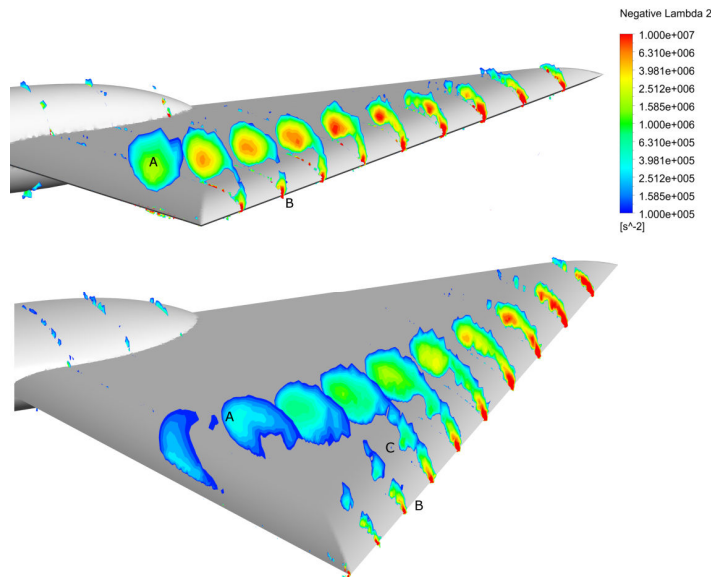


**Fig. 10. Contours of the Negative Part of  $\lambda$ -2, Taken at Spanwise Cross Sections for a  $65^\circ$  (Top) and  $45^\circ$  (Bottom) Sweep Delta Wing.**

**Table 1. Non-dimensionalised Pitching Moment and Forces at Different Sweep Angles. Pitching Moments are Taken about the Mean Aerodynamic Chord of the Wing.**

Sweep Angle	Coefficient of pitch	Coefficient of lift	Coefficient of drag
65°	0.0504	0.3962	0.0779
60°	0.0692	0.4002	0.0883
55°	0.0882	0.4678	0.0952
50°	0.1051	0.4902	0.0997
45°	0.1306	0.4657	0.0971
43°	0.1349	0.4606	0.0969

The coefficients of lift and drag both peak at an angle of sweep of 50°, which corresponds with the angle at which the vortex was observed to begin detaching from the leading edge. While this highlights the impact of the change in vortex behaviour for observed around this sweep angle, it should be noted that this does not mean that wings with this sweep angle are better at generating lift however, as the optimal angle of attack for different sweep angles will differ. High sweep angle wings perform well at higher angles of attack, at which low sweep angle wings experience stall.

## 6. Conclusions

RANS simulations were found to produce accurate predictions of vortex structures on sharp leading edge delta wings with a range of sweep angles at an angle of attack of 10°. As the sweep angle was decreased a weak vortex formed between the leading edge and the primary vortex, with the primary vortex detaching from the leading edge. This occurred at sweep angle of 50° and less, although the effect was most pronounced for angles of 45° and under and resulted in a significant loss of lift on the outer part of the wing. The detachment of the leading edge vortex resulted in an increase in pitch moment.

## Acknowledgments

Some of the experimental data in this paper was provided by Deutsches Zentrum fuer Luft-und Raumfahrt (DLR), the German Aerospace Center, and has been obtained within the International Vortex Flow Experiment-2 (VFE-2).

## References

1. Délery, J. (1992) Physics of vortical flows. *Journal of Aircraft*, 29(5), 856-876.
2. Younis, Y.; Bibi, A.; Haque, A.; and Khushnood, S. (2009). Vortical flow topology on windward and leeward side of delta wing at supersonic speed. *Journal of Applied Fluid Mechanics*, 2(2), 13-21
3. Wong, M.; McKenzie, G.; Ol, M.; Petterson, K.; and Zhang, S. (2006). Joint TTCP CFD studies into the 1303 UCAV performance: First year results. In *24<sup>th</sup> AIAA Applied Aerodynamics Conference*.

4. Arthur, M.; and Petterson, K. (2007). A computational study of the low-speed flow over the 1303 UCAV configuration. *25th AIAA Applied Aerodynamics Conference*.
5. Brett, J.; Tang, L.; Hutchins, N.; Valiyff, A.; and Ooi, A. (2010). Computational fluid dynamics analysis of the 1303 unmanned combat air vehicle. In *17<sup>th</sup> Australasian Fluid Mechanics Conference*, 341-344.
6. Earnshaw, P. (1965). *Measurements of vortex-breakdown position at low speed on a series of sharp-edged symmetrical models*. Technical Report C. P/ No. 828, Ministry of Aviation (London), Aeronautical Research Council.
7. Earnshaw, P.; and Lawford, J. (1964). Low-speed wind tunnel experiments on a series of sharp-edged delta wings. *Technical Report Reports and Memoranda No. 3424*, Ministry of Aviation (London), Aeronautical Research Council.
8. Ol, M.; and Gharib, M. (2003) Leading-edge vortex structure of nonslender delta wings at low Reynolds number. *AIAA Journal*, 41(1), 16-26.
9. Chu, J.; and Luckring, J. (1996). Experimental surface pressure data obtained on 65 delta wing across reynolds number and mach number ranges; Volume 1 - sharp leading edge. *Technical Report Technical Memorandum 4645*, NASA.
10. Konrath, R.; Klein, C.; and Schröder, A. (2008). PSP and PIV investigations on the vfe-2 configuration in sub- and transonic flow. In *Proceedings of 46<sup>th</sup> AIAA Aerospace Sciences Meeting and Exhibit*, Paper AIAA 2008-379.
11. Menter, F. (1994). Two-equation eddy-viscosity turbulence models for engineering applications. *AIAA Journal*, 32(8), 1598-1605.
12. Tullapurka, E.G. (1997). Turbulence models for the computation of flow past airplanes. *Progress in Aerospace Sciences*, 33(1), 71-165.
13. Spalart, P.; and Allmaras, S. (1992). A one-equation turbulence model for aerodynamic flows. *Proceedings of the 30<sup>th</sup> AIAA Aerospace Sciences Meeting and Exhibit*, Reno, United States of America.
14. Jeong, J.; and Hussain, F. (1995). On the identification of a vortex. *Journal of Fluid Mechanics*, 285, 69-94.
15. The Second International Vortex Flow Experiment (VFE-2). Retrieved October 15, 2013, from <http://vfe2.dlr.de/>